

Observation and mitigation of image distortion in high energy electron radiography*

Hao-Qing Li,¹ Liang Sheng,^{2,†} Chang-Qing Zhang,¹ Ying-Chao Du,^{1,‡} Zheng Zhou,^{3,§} Xiu-Feng Weng,² Jia-Hao Xiao,^{4,5} Hong-Qiao Yin,² Bin Sun,² Kun Wei,² Yang Li,² Bao-Jun Duan,² Yong-Tang Liu,² Yan-Hong Zhang,² Mei Zhang,² Yan Song,² Xiao-Dong Zhang,² Jun Liu,² Zhu-Ming Fu,² Qing Xu,² Xue Du,¹ Jian-Peng Gao,¹ Xin-Yi Wang,² Xin-Jian Tan,² and Dong-Wei Hei²

¹Department of Engineering Physics, Tsinghua University, Beijing 100084, China

²State Key Laboratory of Intense Pulsed Radiation Simulation and Effect,
Northwest Institute of Nuclear Technology, Xi'an 710024, China

³Institute of Applied Electronics, China Academy of Engineering Physics, Mianyang 621900, China

⁴Institute of Intelligent Machines, Hefei Institutes of Physical Science, Chinese Academy of Sciences, Hefei 230031, China

⁵Zhongke Hefei Institutes of Collaborative Research and Innovation for Intelligent Agriculture, Hefei 231131, China

Image distortion caused by the angular misalignment of quadrupole magnets in high-energy electron radiography has been studied systematically. We propose that the distortion originates from the coupling of the electron motions in the transverse directions, based on a theoretical analysis and the transfer-matrix method. The relative angular rotation between the second and third magnetic quadrupoles was identified as the main contributor to image distortion. This was verified by both a beam-dynamics simulation and experiments. Different strategies to mitigate this image distortion are also explored, including online magnet tuning using a higher beam energy and a greater magnification factor. This study provides criteria for designing experiments and paves the way for achieving higher image precision.

Keywords: Misalignment, Angular rotation, Russian Quadruplet, Transfer matrix

I. INTRODUCTION

High-energy density physics (HEDP) is the study of matter under extreme pressure and temperature conditions. Under these conditions, the hydrodynamic response results in a high expansion velocity of the order of microns per nanosecond. This therefore requires a diagnostic method with, simultaneously, a temporal resolution ranging from nanoseconds to picoseconds and a spatial resolution $<1\text{ }\mu\text{m}$. Charged particle radiography has developed over decades [1–3]. High energy electron radiography (HEER), one instance of this method, is attracting growing interest for its combination of potential high spatiotemporal resolution, accessibility, and ease of manipulation. HEER has been proposed for use in high-intensity heavy-ion accelerator facilities at the forefront of HEDP science [4, 5]. The basic idea of HEER is to use a set of magnetic quadrupoles to focus the scattered electrons passing through an object to form a point-to-point image on the detector plane. Since its proof-of-principle demonstration at the Los Alamos National Laboratory [6], significant efforts have been made to improve its performance, e.g., by including a higher-brightness electron source and an advanced electron-imaging optics design [7, 8]. The application of high-quality beams with a low energy spread, low emittance, high brightness, and short bunch length generated by state-of-the-art S-band photoinjectors has made significant progress in pushing the spatial resolution to the micron level [9]. Recently, a pioneering high spatial resolution of $0.8\text{ }\mu\text{m}$ was achieved with

a radio-frequency (rf) thermionic cathode gun at the Institute of Modern Physics, which provides high-flux electron beams with a low energy spread and ensures an excellent signal-to-noise ratio in the acquired images [10, 11].

Meanwhile, upgrading and optimizing the imaging system (for example by using elaborately designed quadrupoles and cascaded image units) also play an important role in achieving better spatial resolutions and expanding the scope of application [12, 13]. In particular, the use of a permanent magnet quadrupole (PMQ), with its appealing high gradient, allows a shorter focal length. This is beneficial for making the entire imaging system more compact and increasing the magnification factor [14–16]. Additional advantages are its lower cost, non-restriction from the thermal effect, and fluctuation of current [17, 18]. However, drawbacks of PMQs include demagnetization by radiation, stronger higher-order multiple fields, and sensitivity to misalignment, which degrade image accuracy and even cause serious deterioration of the image quality [19–21]. For example, image skewing was observed at the University of California Los Angeles (UCLA) when using a 4 MeV electron beam focused by a PMQ triplet [22]. Mitigating these defects is therefore crucial to further improve image quality.

In this paper, we report on the image distortion caused by the angular misalignment of PMQs in the Russian quadruplet (RQ) system, and propose strategies to mitigate it. Section II presents the experimental design and the observed phenomena. Their possible explanations are discussed and, eventually, identified with PMQ misalignment. Section III analyzes the origin of the distortion using the transfer matrix and performs start-to-finish simulations to validate the analysis. We also evaluate the influence of different misalignment modes and provide an upper tolerance limit for misalignment. Section IV demonstrates the feasibility of online tuning to correct misalignments in simulations and experiments. Finally, the

* This work was supported by the National Natural Science Foundation of China (Nos. 12005211 and 12075192).

[†] Corresponding author, shengliang@tsinghua.org.cn

[‡] Corresponding author, dych@mail.tsinghua.edu.cn

[§] Corresponding author, z-zhou14@tsinghua.org.cn

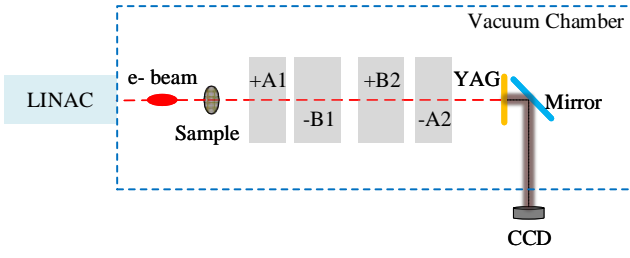


Fig. 1. (Color online) Schematic of the experiment setup. Electrons penetrating the sample are focused by four PMQs placed antisymmetrically with their focusing direction alternating, as denoted by ‘ $\pm A/B$ ’, where ‘ \pm ’ denotes focusing or defocusing and ‘ A/B ’ represents PMQs with different lengths. The point-to-point image is formed on the YAG screen and then deflected to the camera by a mirror.

impacts of different factors in optical design, including the field gradient, beam energy, and magnification, are discussed and strategies are proposed accordingly.

II. EXPERIMENT DESIGN AND RESULTS

The experiment was performed using the Xi’an 120 MeV linear accelerator. Electron beams with tunable time structures were generated in an S-band photocathode rf-gun and then accelerated by two 3-m-long traveling-wave accelerating tubes. The energy was tuned from 30 to 120 MeV. A set of electromagnetic quadrupoles and correctors was used to focus and match the beam [23]. Beams with a 400 pC bunch charge, 10 ps pulse duration, 1 mm.mrad normalized emittance, and 0.1% energy spread were obtained at the entrance of the imaging system chamber. The imaging system consisted primarily of a quadruplet, as commonly used in HEER for its convenience in achieving equal focal lengths and magnifications in the x - and y -directions [24, 25]. An aperture placed in the Fourier plane, where the scattering angle was transformed into a transverse distribution, blocked electrons with a larger scattering angle, resulting in a lower transmittance in the image plane. A 100 μm -thick high-resolution yttrium-aluminum-garnet (YAG) screen was used to convert the electron profile distribution to a visible-light image. The image was reflected onto a lens-coupled CCD placed perpendicular to the beamline using a mirror to avoid radiation damage. All the imaging system equipment (except the lens-coupled CCD) was placed in a vacuum chamber as shown in Fig. 1.

The imaging optics used in our experiment were similar to those in [14], where four PMQs were used to form a RQ. Unlike the two sets of PMQs with different gradients and magnet lengths used in Ref. [14], our experiment used identical gradients for all the PMQs, thereby facilitating the fabrication process and ensuring better uniformity. As their gradients are fixed, the PMQ positions become the only tunable parameters. These were optimized using the high-order beam trans-

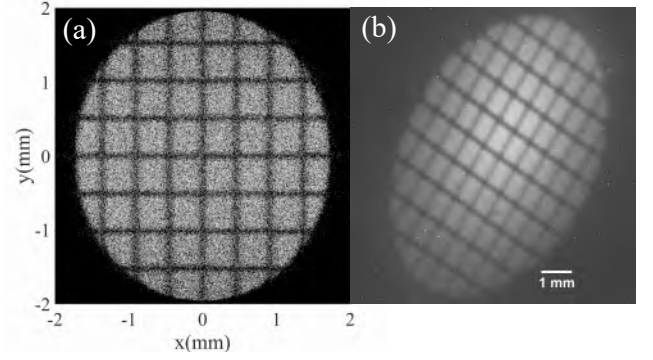


Fig. 2. (Color online) Beam pattern in the image plane: (a) simulation and (b) experiment.

port code COSY INFINITY [26], which describes the fringe field using a six-parameter Enge function. In the experiment, the parameters were adjusted using several remote-controlled custom stages with micron-level precision. The parameters for a 30 MeV beam energy and magnification factors -1.85 and -1.96 in the horizontal and vertical planes, respectively, are listed in Table 1. The positions were calculated from the center of the magnet to the object plane.

TABLE 1. RQ parameters used in the experiment with 30 MeV electrons.

Parameter	Length (mm)	Gradient (T/m)	Position (mm)
A1	13.47	191.4	22.4
B1	20.15	-186.8	49.3
B2	20.12	188.9	97.3
A2	13.64	-189.4	124.3

Simulations were performed before the experiments to validate the effectiveness of the optimized parameters. A Monte Carlo simulation of electrons penetrating a standard 100-mesh copper transmission electron microscopy (TEM) grid (pitch width 300 μm , hole width 260 μm , and bar width 40 μm) with a thickness of 50 μm was performed using GEANT4 [27]. The ASTRA code [28] was employed to conduct a beam-tracking simulation of the imaging system using the measured PMQ field maps. With a 0.2 mm radius collimator placed in the Fourier plane, a clear magnified image of the grid is expected, as shown in Fig. 2(a), 120.84 mm downstream of A2. This result confirms the formation of the point-to-point image of an object.

However, there are always discrepancies between the experimental and ideal designs. After fine-tuning the beam and the quadrupole positions, a representative single-shot image was obtained in the experiment, as shown in Fig. 2(b). The image is clear and some small contaminants are discernible. In spite of not applying a collimator in the experiment, the small magnet apertures worked equivalently to form an image contrast. On the other hand, the image is rotated clockwise by approximately 30° and the magnification factors are -2.26 and -3.06 in the horizontal and vertical planes, respectively.

As mentioned previously, some common factors may cause

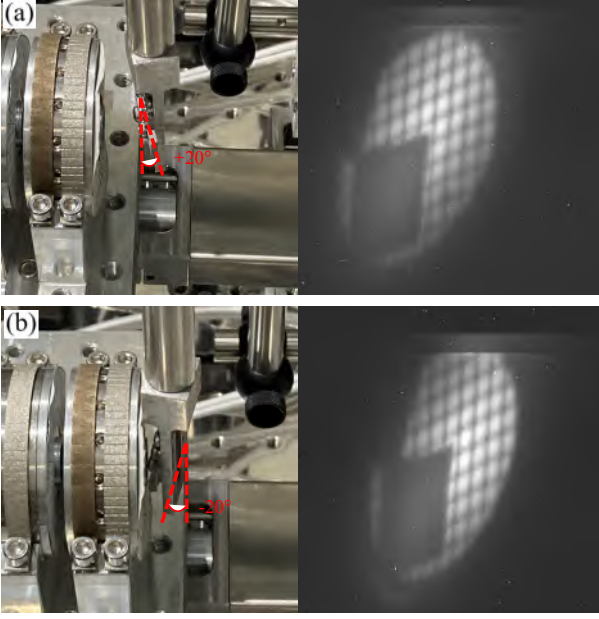


Fig. 3. (Color online) Images of the target rotated by 20° (a) counter-clockwise and (b) clockwise. A square copper patch in the lower-left region is imaged as a rhombus on the screen.

image distortion. Here, we present how these were eliminated in the experiment. First, because the distortion of our pattern appears similar to that observed at UCLA [22], the possibility of sample misplacement had to be excluded. Therefore, the sample was carefully checked before and after shooting to ensure it was set perpendicular to the beam longitudinal axis. We also tested deliberately orienting the grid at an angle of up to $\pm 20^\circ$ relative to the transverse plane of the beamline. The measurements showed that the leaning direction was independent of the sample rotation, thus excluding the possibility of image distortion induced by sample rotation, as shown in Fig. 3. Second, the light path of the image-collecting system (including the mirror- and the lens-coupled CCD) was calibrated before conducting the experiment by imaging a standard calibration grid marker. Third, a misalignment of the beam trajectory relative to the magnetic-field center blurs and shifts the image. Hence, a HeNe laser copropagating with an electron beam was used to prealign the sample and quadruplet along the beamline axis. This was further mitigated by comparing the beam positions when the PMQs were moved into and out of the beamline individually. This was designed to emulate the transverse deflection experienced by the beam when its trajectory deviates from the magnetic center of the PMQs. In addition, optics calculations predicted unequal magnification along the perpendicular axes. Although the predicted effect is not as prominent as we observed, it causes image stretching instead of rotation.

Angular misalignment arises because the quadrupole magnetic field has only two symmetry planes, in contrast to the circular symmetrical field of a solenoid (round lens). Furthermore, the small PMQ aperture (8 mm in the present case)

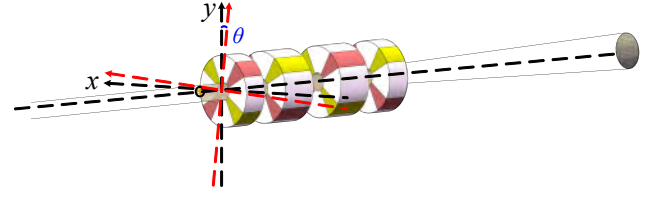


Fig. 4. (Color online) Magnetic field axis (red dashed arrows) orientation of the first magnet, with azimuthal angle θ relative to the beam transverse axis (black dashed arrows).

causes manufacturing, measurement, and alignment difficulties. Typically, the error in the magnetization direction of the magnet segments is approximately $\pm 1^\circ$ in manufacturing. The measurement error of the magnetic field is on the same scale, limited by the size of the Hall probe. Angular misalignment between the quadrupoles causes changes in the force experienced by the particle, making its trace change in consequence. The following section tests this hypothesis by investigating the influence of angular misalignment on radiography.

III. THEORETICAL ANALYSIS AND SIMULATION

A simple example of PMQs with angular misalignment is presented in Fig. 4. The transfer matrix of a quadrupole magnet with angular rotation θ can be written

$$M_\theta = R_{-\theta} M_o R_\theta, \quad (1)$$

with

$$M_o = \begin{pmatrix} \cos KL & \frac{\sin KL}{K} & 0 & 0 \\ -K \sin KL & \cos KL & 0 & 0 \\ 0 & 0 & \cosh KL & \frac{\sinh KL}{K} \\ 0 & 0 & K \sinh KL & \cosh KL \end{pmatrix},$$

$$R_\theta = \begin{pmatrix} \cos \theta & 0 & \sin \theta & 0 \\ 0 & \cos \theta & 0 & \sin \theta \\ -\sin \theta & 0 & \cos \theta & 0 \\ 0 & -\sin \theta & 0 & \cos \theta \end{pmatrix},$$

where $K^2 = G/B\rho$, $B\rho$ is the magnetic rigidity related to the charge-mass ratio and the particle energy, G is the field gradient, and L is the effective magnetic field length of the PMQ. Since $\theta \ll 1$, Eq. 1 can be rewritten as

$$M_\theta = M_o + \theta \Delta M,$$

where

$$\Delta M = \begin{pmatrix} 0 & M_x - M_y \\ M_y - M_x & 0 \end{pmatrix}. \quad (2)$$

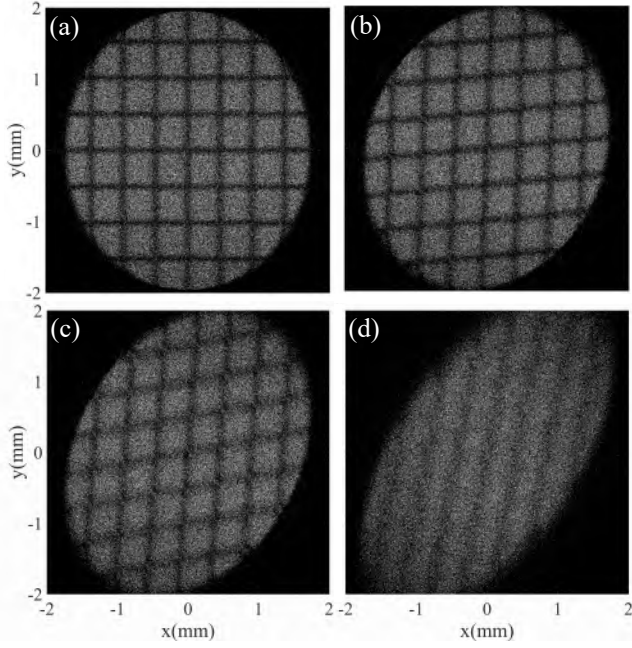


Fig. 5. Image rotation increases with the rotation angle of PMQ B1: (a) $\theta = 0^\circ$, (b) $\theta = 1^\circ$, (c) $\theta = 2^\circ$, (d) $\theta = 5^\circ$.

M_x and M_y are the two upper-left and lower-right 2×2 matrices of M_o , respectively. The entire transfer matrix of the RQ system with the i th magnet rotated by θ is obtained as

$$M_\theta^{\text{total}} = M_o^{\text{total}} + \theta M_{I-M_i} \Delta M_i M_{M_i-O}. \quad (3)$$

Here, M_o^{total} is the total transfer matrix without misalignment, M_{M_i-O} is the transfer matrix from the object plane to the i th magnet, and M_{I-M_i} is the transfer matrix from the i th magnet to the image plane. A similar result can be obtained computationally in more complex situations. The matrix shows that the electron motions in the x - and y -directions are coupled, yielding nonzero upper-right and lower-left matrix elements (in particular M_{13} and M_{31}) and causing image rotation and blurring.

Simulations of the rotated PMQs were performed to verify this prediction. For simplicity, we first considered a situation in which only magnet B1 was rotated by an angle θ ranging from 1° to 5° . The results are presented in Fig. 5. The evolution of the image was reasonably consistent with the experimental results. Distortion arises rapidly with an increase in θ , and the image is barely recognizable when θ reaches 5° . However, an incongruity remains in so far as the mesh is a rhombus in the simulation but rectangular in the experimental results, as shown in Fig. 2(b). This was because the sample shown in Fig. 2(b) is set with a rotation that coincides with the direction of the image rotation, as can be verified by comparison with Fig. 3.

We next discuss the upper limit of the acceptable misalignment for the purpose of guiding experimental design. The angular misalignment of each magnet, despite being random, can be represented in terms of seven modes for the RQ system. The direction of rotation is denoted ‘N’ (clockwise) or

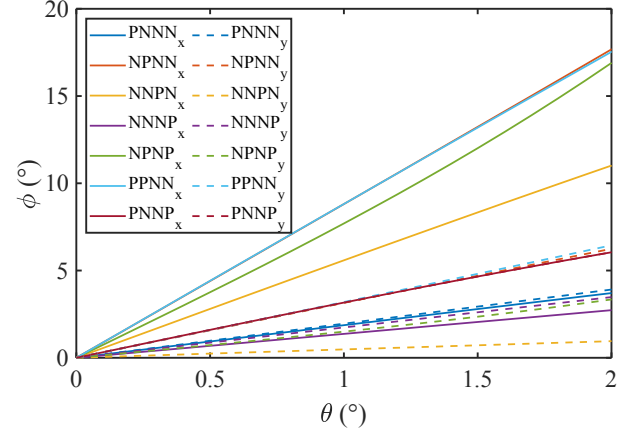


Fig. 6. (Color online) Relation between ϕ and θ for different angular misalignment modes. Solid lines represent ϕ in the x -direction and dashed lines in the y -direction.

‘P’ (counterclockwise), as listed in Fig. 6 and Fig. 7, where each letter represents a magnet from A1 to A2 corresponding to Fig. 1(b)). The rotation angle of the image is defined as ϕ to quantify the rotation level:

$$\phi = \arctan \frac{y_{\text{rot}}}{x_{\text{rot}}} - \arctan \frac{y}{x}, \quad (4)$$

where $(x_{\text{rot}}, y_{\text{rot}})$ is the distorted position and (x, y) is the unperturbed position. With the expanded expressions in Eq. 2 (which can be derived computationally), $y_{\text{rot}}/x_{\text{rot}}$ is coupled in the x and y directions. This results in ϕ varying in different directions, which explains why the stripes are nonperpendicular to each other, as illustrated in Fig. 5. To compare the influence of different magnet rotations, the image rotation ϕ in the x - and y -directions of the different modes was calculated, as depicted in Fig. 6. The most significant influence is displayed by the ‘PNNN’ and ‘NPNN’ modes. Setting the image rotation, shown in Fig. 5(b), as the upper limit, the acceptable angular misalignment of this RQ system becomes $\pm 0.5^\circ$, since only B1 with a 1° rotation is equivalent to the ‘NPNN’ mode with a 0.5° rotation. A comparison of the first four modes shows that B1 and B2 have a stronger impact. This is reasonable, considering their greater lengths. Upon closer inspection, the image rotation is very sensitive to the relative rotation between B1 and B2, in all of these cases. On the other hand, they all show a larger ϕ in the x -direction than in the y -direction except for the ‘PNNN’ and ‘NNNP’ modes. This indicates that setting the concerned feature of the target along with the y -direction is recommended to minimize the detriment.

To estimate the image blur quantitatively, the image error σ is defined as

$$\sigma = \frac{\sum_{n=1}^N \sqrt{\frac{(x_{\text{rot}} - x)^2 + (y_{\text{rot}} - y)^2}{x^2 + y^2}}}{N}, \quad (5)$$

where N denotes the number of electrons in the beam pulse. The relationship between σ and θ for different modes is

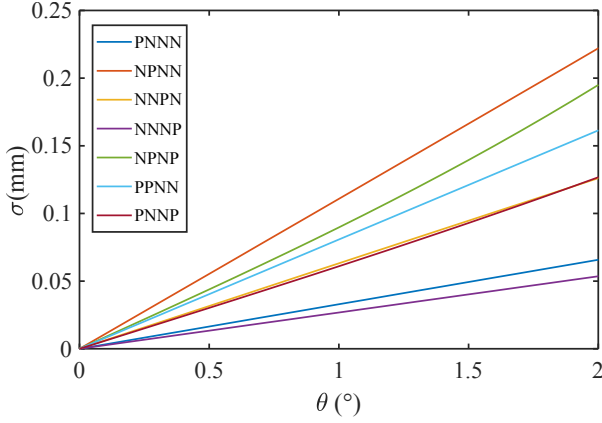


Fig. 7. (Color online) Relation between σ and θ for different angular misalignment modes.

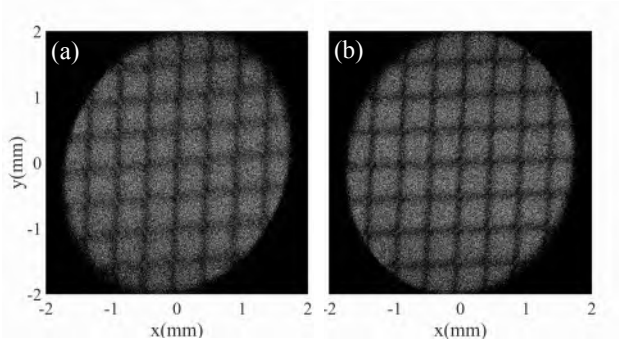


Fig. 8. Distorted image of (a) the NPNN mode with $\theta = 0.65^\circ$ and (b) the PNNP mode with $\theta = 0.95^\circ$.

shown in Fig. 7. A clear trend shows the image error σ increasing almost linearly with θ . Setting the value of σ , as shown in Fig. 5(b), as the upper bound to judge the recognizability of the image, the tolerance of the entire RQ system becomes $\pm 0.5^\circ$. To verify the reliability of the analysis, we simulated the two most complicated misaligning modes, ‘NPNN’ and ‘PNNP’, with θ as their upper limit, as shown in Fig. 8. As expected, this image is similar to that in Fig. 5(b), and the image on the right shows a weaker rotation, since the ‘PNNP’ mode has a lower growth in ϕ , as apparent in Fig. 6.

IV. STRATEGIES FOR MITIGATING THE INFLUENCE OF ANGULAR MISALIGNMENT

A. Online correction

Given the unavoidability of fabrication, assembly, and measurement defects, we here discuss possible remedies for these experiments. The above analysis identified the relative rotation between B1 and B2 as the most significant factor. This provides clues for mitigating the influence of angular misalignment. In the experiment, the beam pattern is moni-

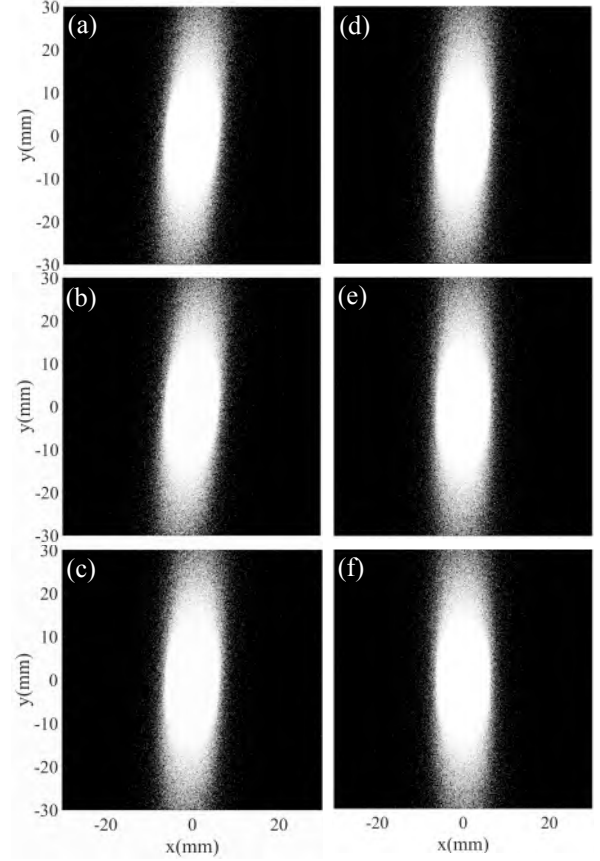


Fig. 9. Simulated beam pattern with only B1 present in the beamline. The rotation angle of B1 decreases from (a) 5° to (f) 0° .

tored instantaneously using a lens-coupled CCD. PMQs can be moved in and out of the beamline in stages with a precision as high as $1\ \mu\text{m}$. When only one magnet is present in the beamline, a fine-tuned beam with a round profile originating from the LINAC is stretched in the defocusing direction and compressed in the focusing direction of the quadrupole magnetic field. A good alignment of the second magnet with the first causes a change in the beam pattern, but the direction of stretching and compression remains constant (or exchanges). However, an angular misalignment between the two magnets causes a rotation of the directions. Therefore, the magnets can be adjusted by observing the evolution of the beam patterns as they move into the beamline individually to mitigate the angular misalignment.

This process was demonstrated by simulating changes in the beam pattern while only B1 remained in the beamline and all other parameters were set to their designed values. The results are shown in Fig. 9. The beam pattern is oblique when B1 is initially rotated by 5° . After correcting for this angle, the beam pattern returns to the vertical orientation. This simulation yields an angular resolution better than 1° without a further evaluation of the images.

The image in Fig. 10 was obtained experimentally. Only a part of the beam pattern is captured owing to the limited

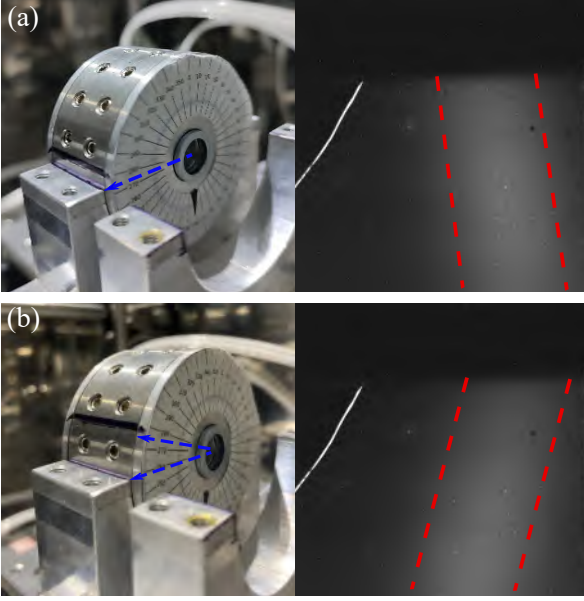


Fig. 10. (Color online) Beam pattern produced with only B1 present in the beamline. (a) The beam pattern leans leftward initially. (b) A clockwise rotation of magnet rotates the stretching direction of the pattern clockwise correspondingly. The bright curve on the YAG screen is caused by a crack.

YAG screen size. Figure 10(a) shows the beam pattern produced with only B1 present in the beamline and with the three other magnets displaced, immediately after the image in Figure 2(b) was taken. The stretching direction leans leftward, confirming the existence of an angular misalignment. A manual rotation of B1 rotates the stretch direction clockwise. Owing to the lack of remote-controlled high-precision rotational stages, a corrected image of the TEM grid was not obtained in this experiment. However, the available results suffice to demonstrate its feasibility. By using an image processing program, a higher-precision correction is achievable. However, that analysis and its practical application are beyond the scope of this study.

B. Higher beam energy

In addition to online tuning, the optimization of the optical design is crucial. The use of different beam energies enables the extraction of different target data, such as the mass density and the electromagnetic field strength [29, 30]. On the one hand, a wide gap between the magnets allows the convenient insertion of a collimator; on the other hand, a compact system is necessary when space is limited. Therefore, quadrupole spacings and lengths deserve due attention in experimental design. We investigated the influence of different factors on the angular-misalignment sensitivity of our system for a fixed magnification.

According to the expanded (computationally derivable) expressions in Eq. 3, the magnifications M_{11} and M_{33} remain constant when the magnet lengths and spaces are scaled in-

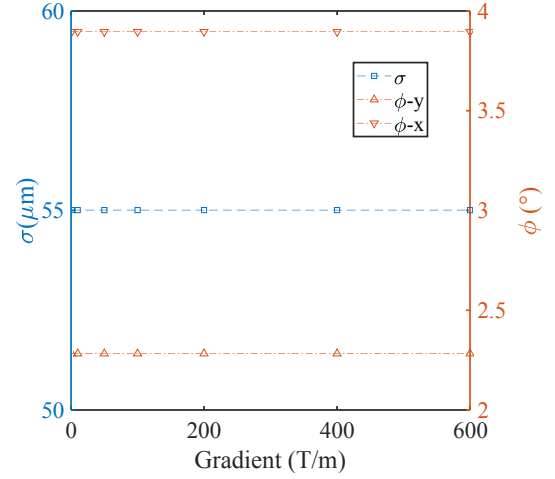


Fig. 11. (Color online) Image error and rotation plotted as functions of the gradient for a given beam energy and magnification. B1 was rotated by 1° to represent an error source.

versely with K , which is proportional to the square root of the field gradient when the beam energy is fixed. Furthermore, the error source factors M_{13} and M_{31} are related only to the rotation angle θ in this case. This indicates that image error σ is independent of the gradient. The same conclusion for the image rotation angle ϕ can be derived by a similar analysis. We verified the prediction with a numerical illustration by setting the beam energy to 30 MeV and fixing the magnification at -7.65 . The other parameters, including the lengths and distances, were recalculated and B1 was rotated by 1° to represent an error source. Figure 11 plots the image error σ and the image rotation angle ϕ as functions of the quadrupole gradient G . The independence of these quantities to the gradient allows greater flexibility in the optical design because the sensitivity to angular misalignment is not increased by the choice of the field gradient.

The same magnification can be achieved at different beam energies by tuning the distance. The beam optics are re-designed accordingly to satisfy the requirement of a point-to-point image with a fixed magnification of -7.65 , using the same set of PMQs with gradient of 200 T/m in Fig. 11. We considered quadrupole B1 with a rotation angle of 1° to represent a distortion source. The image error σ and rotation ϕ , plotted in Fig. 12, show a rapid drop with increasing beam energy. However, the trend slows down substantially for energies beyond 200 MeV. This also explains why the distortion in the case of a higher beam energy of 45 MeV with the same set of PMQs was not as apparent in previous experiments as in the present results [31]. Thus, a higher beam energy is recommended to mitigate the influence of misalignment in scenarios where the penetration ability is not a major factor.

C. Larger magnification

Different magnifications can be achieved using a given magnetic lens and beam energy by tuning the object-image

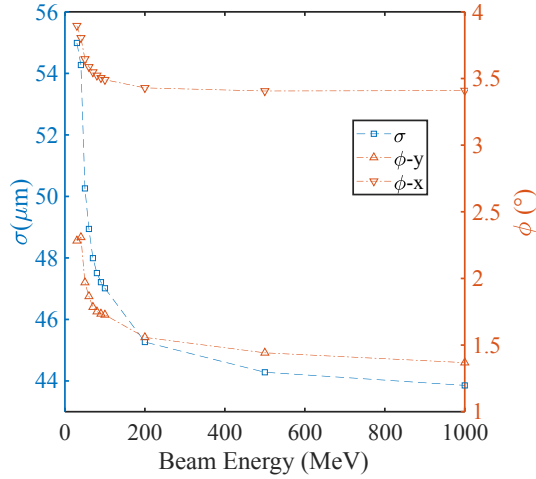


Fig. 12. (Color online) Image error and rotation plotted as functions of the beam energy, for a given set of PMQs and magnification. B1 was rotated by 1° to represent an error source.

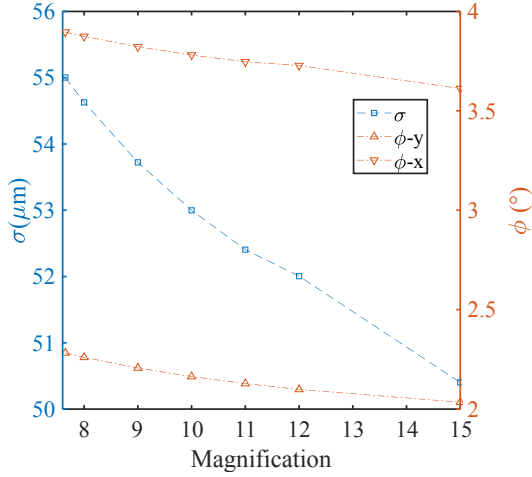


Fig. 13. (Color online) Image error and rotation plotted as functions of the magnification, for a given set of PMQs and beam energy. B1 is rotated by 1° to represent an error source.

separation. This makes it convenient to locate the target and to zoom in to obtain a detailed characterization. Because the

beam energy and lens parameters are fixed, M_{11} , M_{33} , M_{13} , and M_{31} are observed to be proportional to the image distance. However, the absolute values of the coefficients in M_{11} and M_{33} are greater than M_{13} and M_{31} . Consequently, the numerator grows more slowly than the denominator of the term under the square root of Eq. 5. Thus, the image error decreases by increasing the image distance, which also increases the magnification. The dependences of the image error and rotation on the magnification, plotted in Fig. 13, validate the analysis. Hence a larger magnification is recommended, and it is also desired usually.

V. SUMMARY

In conclusion, the image distortion observed in PMQ-based high-energy electron radiography can be explained by the angular misalignment of PMQs, which leads to the coupling of electron motions in the x- and y-directions. Simulations and experiments validated our analysis, and the influence of different factors was studied in detail. Theoretical analysis shows that the relative rotation between B1 and B2 in an RQ system has the most significant impact. This motivates a more careful consideration of fabrication and assembly. In addition, limiting the angular misalignment of each quadrupole to $\pm 0.5^\circ$ is necessary to avoid fatal distortion. The feasibility of the online tuning of the magnets individually, based on the beam pattern, to correct the misalignment was verified experimentally. A higher beam energy and a greater magnification also help to mitigate the misalignment. In addition, the gradient analysis justifies the compacting of the imaging system without increasing the distortion. Further work, including the introduction of an image processing program and rotational stages, is required to achieve higher precision adjustments in future experiments. Most of the considerations can be extended to designs utilizing different types of quadrupole systems. This method may be useful in other applications such as beam-based alignment and beam characterization [32, 33].

ACKNOWLEDGMENTS

The authors thank the staff of the Xi'an 120 MeV linear accelerator of the Northwest Institute of Nuclear Technology for their support during the experiments.

-
- [1] N. S. P. King, E. Ables, Ken Adams, *et al.*, An 800-MeV proton radiography facility for dynamic experiments. Nucl. Instrum. Meth. A. **424**, 84-91 (1999). doi:10.1016/S0168-9002(98)01241-8
 - [2] A. A. Golubev, V. S. Demidov, E. V. Demidova, *et al.*, Application of TWAC beams for diagnostics of fast processes. Atom. Energy. **104**, 134-141 (2008). doi:10.1007/s10512-008-9004-2
 - [3] C. L. Morris, N. S. P. King, K. Kwiatkowski *et al.* Charged particle radiography. Reports on Progress in Physics. **76**, 046301(2013). doi:10.1088/0034-4885/76/4/046301
 - [4] Y. Zhao, R. Cheng, Y. Wang, *et al.*, High energy density physics research at IMP, Lanzhou, China. High Power Laser Science and Engineering. **2**, e39(2014). doi:10.1017/hpl.2014.44
 - [5] Q. Zhao, Y. Ma, J. Xiao, *et al.*, Three-Dimensional High-Energy Electron Radiography Method for Static Mesoscale Samples Diagnostics. Applied Sciences. **9**, (2019). doi:10.3390/app9183764
 - [6] F. Merrill, F. Harmon, A. Hunt, *et al.*, Electron radiography. Nucl. Instrum. Meth. B. **261**, 382-386 (2007). doi:10.1016/j.nimb.2007.04.127

- [7] F. E. Merrill, J. Goett, J. W. Gibbs, *et al.*, Demonstration of transmission high energy electron microscopy. *Appl. Phys. Lett.* **112**, (2018). doi:10.1063/1.5011198
- [8] Q. T. Zhao, S. C. Cao, R. Cheng *et al.*, Generation of uniform transverse beam distributions for high-energy electron radiography. *Laser Part. Beams*. **36**, 313-322(2018). doi:10.1017/s0263034618000265
- [9] Z. Zhou, Y. C. Du, S. C. Cao, *et al.*, Experiments on bright field and dark field high energy electron imaging with thick target material. *Phys. Rev. Accel. Beams*. **21**, (2018). doi:10.1103/physrevaccelbeams.21.074701
- [10] Y. L. Zhu, P. Yuan, S. C. Cao, *et al.*, Design and simulation of a LINAC for high energy electron radiography research. *Nucl. Instrum. Meth. A*. **911**, 74-78(2018). doi:10.1016/j.nima.2018.09.133
- [11] Z. H. Ran, Z. P. Li, Q. T. Zhao, *et al.*, Demonstration of high energy electron radiography with sub-micron spatial resolution. *Nucl. Instrum. Meth. A*. **1015**, 165769 (2021). doi:10.1016/j.nima.2021.165769
- [12] M. S. Freeman, J. C. Allison, E. F. Aulwes, *et al.*, Dark field proton radiography. *Appl. Phys. Lett.* **117**, 144103(2020). doi:10.1063/5.0021044
- [13] W. Wan, F. R. Chen, Y. Zhu, Design of compact ultrafast microscopes for single- and multi-shot imaging with MeV electrons. *Ultramicroscopy*. **194**, 143-153(2018). doi:https://doi.org/10.1016/j.ultramic.2018.08.005
- [14] Z. Zhou, Y. Fang, H. Chen, *et al.*, Demonstration of Single-Shot High-Quality Cascaded High-Energy-Electron Radiography using Compact Imaging Lenses Based on Permanent-Magnet Quadrupoles. *Phys. Rev. Applied*. **11**, 034068(2019). doi:10.1103/PhysRevApplied.11.034068
- [15] J. K. Lim, P. Frigola, G. Travish, *et al.*, Adjustable, short focal length permanent-magnet quadrupole based electron beam final focus system. *Phys. Rev. Spec. Top.-Accel. Beams*. **8**, 072401(2005). doi:10.1103/PhysRevSTAB.8.072401
- [16] R. K. Li, P. Musumeci. Single-Shot MeV Transmission Electron Microscopy with Picosecond Temporal Resolution. *Phys. Rev. Applied*. **2**, 024003(2014). doi:10.1103/PhysRevApplied.2.024003
- [17] K. Halbach, Permanent multipole magnets with adjustable strength. *IEEE Trans. Nucl. Sci.* **30**, 3(1982). doi:10.1109/TNS.1983.4336645
- [18] T. Mottershead, D. Barlow, B. Blind, *et al.*, Design and operation of a proton microscope for radiography at 800 MeV. *Proceedings of the 2003 Particle Accelerator Conference*. **1**, 702-704(2003). doi:10.1109/PAC.2003.1289014
- [19] S. Becker, M. Bussmann S. Raith, *et al.*, Characterization and tuning of ultrahigh gradient permanent magnet quadrupoles. *Phys. Rev. Spec. Top.-Accel. Beams*. **12**, 102801 (2009). doi:10.1103/PhysRevSTAB.12.102801
- [20] R. D. Brown, J. R. Cost, Radiation effects in magnetic and superconducting materials. *JOM*. **42**, 39-43 (1990). doi:10.1007/BF03220872
- [21] E. W. Blackmore, Radiation Effects of Protons on Samarium-Cobalt Permanent Magnets. *IEEE Trans. Nucl. Sci.* **32**, 3669-3671(1985). doi:10.1109/TNS.1985.4334463
- [22] D. Cesar, J. Maxson, P. Musumeci, *et al.*, Demonstration of Single-Shot Picosecond Time-Resolved MeV Electron Imaging Using a Compact Permanent Magnet Quadrupole Based Lens. *Phys. Rev. Lett.* **117**, 024801 (2016). doi:10.1103/PhysRevLett.117.024801
- [23] H. Chen, L. Yan, Q. Tian, *et al.*, Commissioning the photoinjector of a gamma-ray light source. *Phys. Rev. Accel. Beams*. **22**, (2019). doi:10.1103/physrevaccelbeams.22.053403
- [24] P. W. Hawkes, *Quadrupoles in Electron Lens Design*. (Academic Press, 1970).
- [25] Y. Zhao, Z. Zhang, W. Gai, *et al.*, High energy electron radiography scheme with high spatial and temporal resolution in three dimension based on a e-LINAC. *Laser and Particle Beams*. **34**, 338-342(2016). doi:10.1017/s0263034616000124
- [26] K. Makino, M. Berz, COSY INFINITY Version 9. *Nucl. Instrum. Meth. A*. **558**, 346-250 (2006). doi:10.1016/j.nima.2005.11.109
- [27] S. Agostinelli, J. Allison, K. Amako, *et al.*, Geant4—a simulation toolkit. *Nucl. Instrum. Meth. A*. **506**, 250-303 (2003). doi:10.1016/S0168-9002(03)01368-8
- [28] K. Floettmann, ASTRA, DESY, <https://www.desy.de/~mpyflo/>
- [29] J. Xiao, Z. Zhang, S. Cao, *et al.*, Areal density and spatial resolution of high energy electron radiography. *Chin Phys B*. **27**, 035202(2018). doi:10.1088/1674-1056/27/3/035202
- [30] J. H. Xiao, Y. C. Du, H. Q. Li, *et al.*, Ultrafast high energy electron lens radiography suitable for transient electromagnetic field diagnosis. *J Instrum*. **17**, P01033(2022). doi:10.1088/1748-0221/17/01/p01033
- [31] Z. Zhou, Research on high spatiotemporal resolution high energy electron imaging and electron diffraction. Dissertation. (2019). doi:10.27266/d.cnki.gqhau.2019.000630(in Chinese)
- [32] L. Zheng, J. Shao, Y. Du, *et al.*, Overestimation of thermal emittance in solenoid scans due to coupled transverse motion. *Phys. Rev. Accel. Beams*. **21**, (2018). doi:10.1103/physrevaccelbeams.21.122803
- [33] G. Manahan, E. Brunetti, C. Aniculaesei, *et al.*, Characterization of laser-driven single and double electron bunches with a permanent magnet quadrupole triplet and pepper-pot mask. *New J. Phys.* **16**, 103006(2014). doi:10.1088/1367-2630/16/10/103006